Viscoelastic flow simulations in disordered porous media

De, S.; Kuipers, J.A.M.; Peters, E.A.J.F.; Padding, Johan

Publication date
2017

Document Version
Final published version

Published in
Proceedings of the 12th International Conference on Computational Fluid Dynamics in the Oil & Gas, Metallurgical and Process Industries

SINTEF
PROCEEDINGS
2

Proceedings of the 12th International Conference on Computational Fluid Dynamics in the Oil & Gas, Metallurgical and Process Industries

Progress in Applied CFD – CFD2017

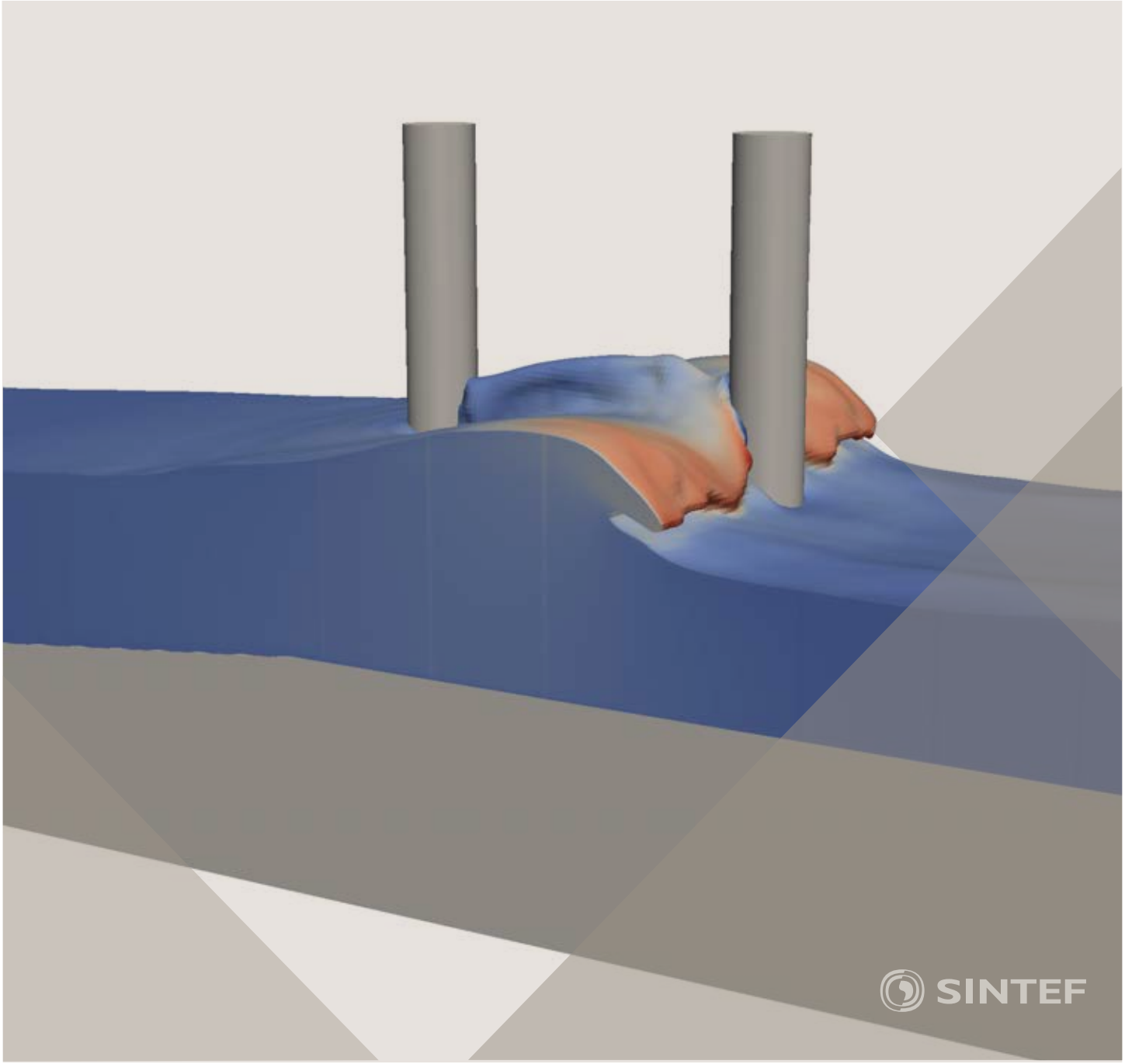

SINTEF

SINTEF Proceedings

Editors:
Jan Erik Olsen and Stein Tore Johansen

Progress in Applied CFD – CFD2017

Proceedings of the 12th International Conference on Computational Fluid Dynamics in the Oil & Gas, Metallurgical and Process Industries

SINTEF Academic Press

SINTEF Proceedings no 2
Editors: Jan Erik Olsen and Stein Tore Johansen
Progress in Applied CFD – CFD2017
Selected papers from 10th International Conference on Computational Fluid Dynamics in the Oil & Gas, Metallurgical and Process Industries

Key words:
CFD, Flow, Modelling

Cover, illustration: Arun Kamath

ISSN 2387-4295 (online)
ISBN 978-82-536-1544-8 (pdf)

SINTEF Academic Press
Address: Forskningsveien 3 B
PO Box 124 Blindern
N-0314 OSLO
Tel: +47 73 59 30 00
Fax: +47 22 96 55 08

www.sintef.no/byggforsk
www.sintefbok.no

SINTEF Proceedings
SINTEF Proceedings is a serial publication for peer-reviewed conference proceedings on a variety of scientific topics.
The processes of peer-reviewing of papers published in SINTEF Proceedings are administered by the conference organizers and proceedings editors. Detailed procedures will vary according to custom and practice in each scientific community.

PREFACE

This book contains all manuscripts approved by the reviewers and the organizing committee of the 12th International Conference on Computational Fluid Dynamics in the Oil & Gas, Metallurgical and Process Industries. The conference was hosted by SINTEF in Trondheim in May/June 2017 and is also known as CFD2017 for short. The conference series was initiated by CSIRO and Phil Schwarz in 1997. So far the conference has been alternating between CSIRO in Melbourne and SINTEF in Trondheim. The conferences focuses on the application of CFD in the oil and gas industries, metal production, mineral processing, power generation, chemicals and other process industries. In addition pragmatic modelling concepts and bio-mechanical applications have become an important part of the conference. The papers in this book demonstrate the current progress in applied CFD.

The conference papers undergo a review process involving two experts. Only papers accepted by the reviewers are included in the proceedings. 108 contributions were presented at the conference together with six keynote presentations. A majority of these contributions are presented by their manuscript in this collection (a few were granted to present without an accompanying manuscript).

The organizing committee would like to thank everyone who has helped with review of manuscripts, all those who helped to promote the conference and all authors who have submitted scientific contributions. We are also grateful for the support from the conference sponsors: ANSYS, SFI Metal Production and NanoSim.

Stein Tore Johansen & Jan Erik Olsen

Organizing committee:

Conference chairman: Prof. Stein Tore Johansen
Conference coordinator: Dr. Jan Erik Olsen
Dr. Bernhard Müller
Dr.Sigrid Karstad Dahl
Dr.Shahriar Amini
Dr.Ernst Meese
Dr.Josip Zoric
Dr.Jannike Solsvik
Dr.Peter Witt

Scientific committee:

Stein Tore Johansen, SINTEF/NTNU
Bernhard Müller, NTNU
Phil Schwarz, CSIRO
Akio Tomiyama, Kobe University
Hans Kuipers, Eindhoven University of Technology
Jinghai Li, Chinese Academy of Science
Markus Braun, Ansys
Simon Lo, CD-adapco
Patrick Segers, Universiteit Gent
Jiyuan Tu, RMIT
Jos Derksen, University of Aberdeen
Dmitry Eskin, Schlumberger-Doll Research
Pär Jönsson, KTH
Stefan Pirker, Johannes Kepler University
Josip Zoric, SINTEF

CONTENTS

VISCOELASTIC FLOW SIMULATIONS IN DISORDERED POROUS MEDIA

S. De, J.A.M. Kuipers, E.A.J.F. Peters
Department of Chemical Engineering and Chemistry, Eindhoven University of Technology, The Netherlands

J.T. Padding*
* Process & Energy department, Delft University of Technology, The Netherlands

E-mail: s.de@tue.nl
j.t.padding@tudelft.nl

ABSTRACT

We investigate creeping flow of a viscoelastic fluid through a three dimensional random porous medium using computational fluid dynamics. The simulations are performed using a finite volume methodology with a staggered grid. The no slip boundary condition on the fluid-solid interface is implemented using a second order finite volume immersed boundary (FVM-IBM) methodology [1]. The viscoelastic fluid is modelled using a FENE-P type constitutive relation. The simulations reveal a transition of flow structure from a laminar Newtonian regime to a nonstationary non-Newtonian regime with increasing viscoelasticity. We find that the flow profiles are mainly governed by the porous microstructure. By choosing a proper length scale a universal curve for the flow transition can be obtained. A study of the flow topology shows how in such disordered porous media shear, extensional and rotational contributions to the flow evolve with increased viscoelasticity.

Keywords: CFD, IBM, Viscoelastic, Porous Media.

NOMENCLATURE

Greek Symbols

ρ Fluid density, [kg/m^3].

η_s Solvent viscosity, [kg/m.s].

η_p Polymer zero shear viscosity, [kg/m.s].

η Total viscosity, [kg/m.s].

Latin Symbols

p Pressure, [Pa].

$\mathbf{u}$ Velocity, [m/s].

$\boldsymbol{\tau}$ Viscoelastic Stress tensor, [Pa].

λ Relaxation time, [sec].

L Maximum dumbbell extensibility.

β Viscosity ratio (η_s / η).

α Solid fraction.

ϕ Void fraction.

d_p Particle diameter, [m].

R_c Particle radius, [m].

N_p Particle Number

k Permeability, [m^2].

ϕ_i Fluid variable.

De Deborah number.

Re Reynolds number.

Sub/superscripts

∇ Second rank tensor.

VE Viscoelastic fluids.

N Newtonian fluids.

INTRODUCTION

The flow of complex fluids through porous media is a field of considerable research due to its wide range of practical applications including enhanced oil recovery, blood flow, polymer processing, catalytic polymerization, bioprocessing, geology [2–4]. The flow of Newtonian fluids though porous media is relatively well understood in the framework of Darcy's law [2]. Also, a significant effort has been made to understand flow through porous media of non-Newtonian fluids with a viscosity that depends on the instantaneous local shear-rate (inelastic non-Newtonian fluids, or quasi-Newtonian fluids), as reviewed by Chhabra et. al. [5] and Savins [6]. However, flow through disordered porous media of viscoelastic fluids, i.e. non-Newtonian fluids displaying elasticity, is far from being understood [5,7,8]. This is due to the complex interplay between the nonlinear fluid rheology and the porous geometry. Several types of numerical frameworks have been used to model flow of non-Newtonian fluids through porous media, including extensions of Darcy's law [9], capillary based models [10], and direct numerical simulations based on computational fluid dynamics. Unfortunately, extensions of Darcy's law and capillary based models are found to be inadequate to capture the complete physics of pore scale viscoelastic flow through porous media [11–13].

Many numerical studies focus on relatively simple geometries to learn about the essentials of non-Newtonian fluid flow through porous media [14–17]. Sometimes a full three-dimensional random porous medium is studied, which is already closer to a realistic pore geometry, but such studies are then usually limited to power-law fluids, which are the most commonly applied quasi-Newtonian fluids [11,18–20]. For example, Morais et al. [18] applied direct numerical simulations

to investigate the flow of power-law fluids through a disordered porous medium. Simulations of fully viscoelastic fluid flows are limited to two dimensional pore geometries [21–25]. It is now commonly agreed that including viscoelasticity is important: both numerically and experimentally, viscoelasticity is found to lead to profound effects such as enhanced pressure drop and elastic instabilities (sometimes referred to as elastic turbulence) [5,26–28]. So, although it is known that viscoelastic fluids behave more complex than inelastic non-Newtonian fluids, the current literatures shows a lack of detailed simulations of fully three dimensional flows of viscoelastic fluids through random porous media.

In this paper, we report on a numerical study of the flow of viscoelastic fluids through three dimensional random porous media consisting of packed arrangements of monodispersed spherical particles using a combined finite volume immersed boundary (FVM-IBM) methodology. Four different porosities are studied for a range of low to high Deborah numbers (defined later). We measure in detail the viscoelastic fluid flow structure and stress development in the porous medium. We will show a transition from a laminar Newtonian flow profile to an instable flow configuration, and will relate it to a strong increase in pressure drop. An analysis of the flow topology will show how shear, extensional and rotational dominated flow regimes change with increasing viscoelasticity for different porous structures. Finally, we will show how the distribution of energy dissipation in the porous medium changes with increasing viscoelasticity and correlate this with the flow topology. This analysis will help us to understand the interplay of pore structure and fluid rheology in three dimensional porous microstructures.

MODEL DESCRIPTION

The fundamental equations for an isothermal incompressible viscoelastic flow are the equations of continuity and momentum, and a constitutive equation for the non-Newtonian stress components. The first two are as follows:

$$\nabla \cdot \mathbf{u} = 0 \qquad (1)$$

$$\rho\left[\frac{\partial \mathbf{u}}{\partial t} + \mathbf{u}\cdot\nabla\mathbf{u}\right] = -\nabla p + 2\eta_s \nabla\cdot\mathbf{D} + \nabla\cdot\boldsymbol{\tau} \qquad (2)$$

The Newtonian solvent contribution is explicitly added to the stress and defined as $2\eta_s\mathbf{D}$, where the rate of strain is $\mathbf{D} = (\nabla\mathbf{u} + (\nabla\mathbf{u})^T)/2$. The solvent viscosity η_s is assumed to be constant. In this work the viscoelastic polymer stress is modeled through the constitutive FENE-P model, which is based on the finitely extensible non–linear elastic dumbbell for polymeric materials, as explained in detail by Bird et al. [29]. The equation is derived from molecular theory, where a polymer chain is represented as a dumbbell consisting of two beads connected by an entropic spring. Other basic rheological models, such as the Maxwell model and Oldroyd–B model, take the elastic force between the beads to be proportional to the separation between the beads. The main disadvantage of such models is that the dumbbell can be stretched indefinitely, leading to divergent behavior and associated numerical instabilities in strong extensional flows. These problems are prevented by the use of a finitely extensible spring. The basic form of the FENE-P constitutive equation is:

$$f(\boldsymbol{\tau})\boldsymbol{\tau} + \lambda \overset{\nabla}{\boldsymbol{\tau}} = 2a\eta_p\mathbf{D},$$

$$\text{with: } f(\boldsymbol{\tau}) = 1 + \frac{3a + (\lambda/\eta_p)\,\mathrm{tr}(\boldsymbol{\tau})}{L^2}, \qquad (3)$$

$$a = \frac{L^2}{L^2 - 3}$$

In equation (3) the operator ∇ represents the upper-convected time derivative, defined as

$$\overset{\nabla}{\boldsymbol{\tau}} = \frac{\partial\boldsymbol{\tau}}{\partial t} + \mathbf{u}\cdot\nabla\boldsymbol{\tau} - \nabla\mathbf{u}^T\cdot\boldsymbol{\tau} - \boldsymbol{\tau}\cdot\nabla\mathbf{u} \qquad (4)$$

In equation (3) $\mathrm{tr}(\boldsymbol{\tau})$ denotes the trace of the stress tensor. The parameter L equals the maximum length of a FENE dumbbell normalized by its equilibrium length. When $L^2 \to \infty$ the Oldroyd–B model is recovered.

We simulate an unsteady viscoelastic flow through a static array of randomly arranged monodisperse spheres, constituting a model porous medium, using computational fluid dynamics (CFD). The primitive variables used in the formulation of the model are velocity, pressure and polymer stress. All the mass and momentum equations are considered and discretised in space and time. A coupled finite volume – immersed boundary methodology [1] (FVM - IBM) with a Cartesian staggered grid is applied. In the FVM, the computational domain is divided into small control volumes ΔV and the primitive variables are solved in the control volumes in an integral form over a time interval Δt.

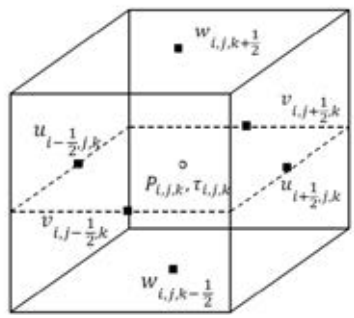

Figure 1. Location of primitive variables in a 3D control volume (fluid cell).

The location of all the primitive variables in a 3D cell are indicated in figure 1.

We apply the discrete elastic viscous stress splitting scheme (DEVSS), originally proposed by Guénette and Fortin [30], to introduce the viscoelastic stress terms in the Navier-Stokes equation because it stabilizes the momentum equation, which is especially important at larger polymer stresses. A uniform grid spacing is used in all directions. The temporal discretization for the momentum equation (2) is as follows,

$$\rho\mathbf{u}^{n+1} = \rho\mathbf{u}^{n} + \Delta t\left\{-\nabla p^{n+1} - \left[\mathbf{C}_f^{n+1} + \left(\mathbf{C}_m^{n} - \mathbf{C}_f^{n}\right)\right] + \left[\left(\eta_s + \eta_p\right)\nabla^2\mathbf{u}^{n+1} + \nabla\cdot\boldsymbol{\tau}^{n}\right] - \mathbf{E}_p^{n}\right\} \quad (5)$$

Here $\eta_p\nabla^2\mathbf{u}^{n+1}$ and $\mathbf{E}_p^n = \eta_p\nabla^2\mathbf{u}^n$ are the extra variables we introduce to obtain numerical stability, where n indicates the time index. $\mathbf{C}$ represents the net convective momentum flux given by:

$$\mathbf{C} = \rho\left(\nabla\cdot\mathbf{uu}\right) \quad (6)$$

Here the first order upwind scheme is used for the implicit evaluation of the convection term (called $\mathbf{C}_f$). In the calculation of the convective term we have implemented a deferred correction method. The deferred correction contribution that is used to achieve second order spatial accuracy while maintaining stability is $\left(\mathbf{C}_m^n - \mathbf{C}^n{}_f\right)$ and is treated explicitly. In this expression $\mathbf{C}_m$ indicates the convective term evaluated by the total variation diminishing min-mod scheme. A second order central difference (CD) scheme is used for the discretization of diffusive terms.

In equation (5) the viscoelastic stress part $\boldsymbol{\tau}$ is calculated by solving equation (3). The viscoelastic stress tensors are all located in the center of a fluid cell, and interpolated appropriately during the velocity updates. The convective part of equation (3) is solved by using the higher order upwind scheme.

Equation (5) is solved by a fractional step method, where the tentative velocity field in the first step is computed from:

$$\rho\mathbf{u}^{**} = \rho\mathbf{u}^{n} + \Delta t\left\{\begin{array}{l}-\nabla p^{n+1} - \left[\mathbf{C}_f^{**} + \left(\mathbf{C}_m^{n} - \mathbf{C}_f^{n}\right)\right] + \\ \left[\left(\eta_s + \eta_p\right)\nabla^2\mathbf{u}^{**} + \nabla\cdot\boldsymbol{\tau}^{n}\right] + \rho\mathbf{g} - \mathbf{E}_p^{n}\end{array}\right\} \quad (7)$$

In equation (7) we need to solve a set of linear equations.

The velocity at the new time step $n+1$ is related to the tentative velocity is as follows:

$$\mathbf{u}^{n+1} = \mathbf{u}^{**} - \frac{\Delta t}{\rho}\nabla\left(\delta p\right) \quad (8)$$

where $\delta p = p^{n+1} - p^{n}$ is the pressure correction. As $\mathbf{u}^{n+1}$ should satisfy the equation of continuity, the pressure Poisson equation is calculated as:

$$\nabla\cdot\left\{\frac{\Delta t}{\rho}\nabla\left(\delta p\right)\right\} = \nabla\cdot\mathbf{u}^{**} \quad (9)$$

We use a robust and efficient block – incomplete Cholesky conjugate gradient (B-ICCG) algorithm to solve the resulting sparse matrix for each velocity component in a parallel computational environment. The solver iterations are performed until the norm of the residual matrix is less than the convergence criteria, which is set at 10^{-14} for our simulations.

As the viscoelastic stress tensor components are coupled amongst themselves and with the momentum equation, the velocity at the new time level $\mathbf{u}^{n+1}$ is used to calculate the stress value accordingly.

No-slip velocity boundary conditions at the interface between the viscoelastic fluid and solid objects are imposed through the immersed boundary method (IBM) at the level of the discretized momentum equations by extrapolating the velocity field along each Cartesian direction towards the body surface using a second order polynomial. To ensure a relatively high accuracy, we use a coupling method which works directly at the level of the discretized momentum equation (5). The discrete representation of the momentum equation is given by

$$a_c\phi_c + \sum_{nb} a_{nb}\phi_{nb} = b_c \quad (10)$$

Where ϕ_i is a fluid phase variable (in this case a component of the fluid velocity). This equation indicates that the value of ϕ_i for a fluid node "c" outside of the immersed object can be related to the values of its neighboring nodes "nb", some of which may lie inside the immersed object.
A schematic representation of this situation is shown in Figure 2.

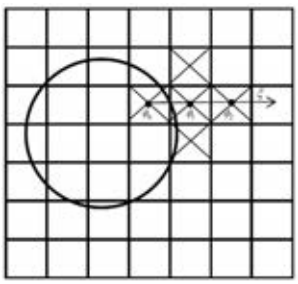

Figure 2. Immersed boundary method implementation strategy for a fluid variable ϕ_i

We use a second order interpolation to describe the value of ϕ_i as a function of the local coordinate (see Figure 2).

This procedure is carried out for all solid nodes to ensure that the boundary condition is properly satisfied for all the solid nodes. The main advantage of using the immersed boundary method is that it requires no conformal meshing near the fluid-solid interface, and the method is computationally robust and cheap.

RESULTS

We employ our method to investigate the flow of viscoelastic fluid through a static array of randomly arranged spherical particles in a 3D periodic domain (figure 3). The domain size is set by the solids volume fraction α, the diameter of each particle d_p and number of particles N_p. To generate the random packing for $\alpha \leq 0.45$, a standard hard sphere Monte-Carlo (MC) method [31] is used. However, such a MC method does not provide sufficiently random configurations in highly dense packings [32]. Thus, to generate random configurations at $\alpha > 0.45$, an event driven method combined with a particle swelling procedure is applied [33]. This ensures the particles are randomly distributed. The same approach was followed by Tang et al. for Newtonian fluid simulations for a range of low to intermediate Reynolds numbers [34].

In all simulations the flow is driven by a constant body force exerted on the fluid in the *x*-direction, while maintaining periodic boundary conditions in all three directions. Simulations of random arrays are carried out with $N_p = 108$ spheres arranged in different configurations. The particle diameter d_p is always kept constant. The solid fractions α investigated are 0.3, 0.4, 0.5 and 0.6, respectively. Porosities therefore range from 0.7 to 0.4.

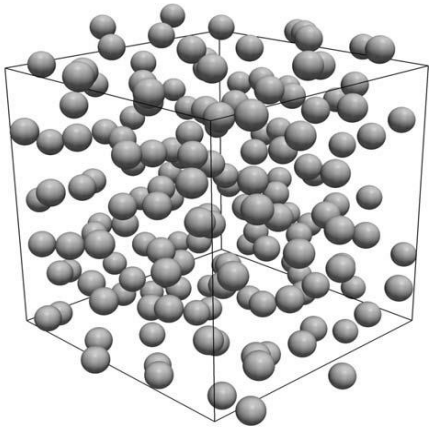

Figure 3. Particle configuration at solid fraction $\alpha = 0.4$ of a random array of monodisperse spheres. Note that the particles are scaled by 50% for better visualization.

For the FENE-P viscoelastic fluid we use a constant extensional parameter (L^2) of 100. The viscosity ratio is kept at 0.33. The λ is kept constant at 40 sec. As we want to study the interaction between the viscoelastic fluid and solid for different flow configurations we keep a constant value of $L^2 = 100$. For reference, we also simulate a Newtonian fluid with the same zero-shear viscosity as the polymer solution. In all our simulations we keep the Reynolds number low, below a value of 0.01, ensuring we are always in the creeping flow regime and any type of inertial effects will be insignificant. Deborah numbed is defined as $\mathrm{De}_R = \lambda U / R_c$, based on the sphere radius and mean flow velocity *U*.

We have performed simulations for three different mesh sizes $\Delta = R_c/30$, $\Delta = R_c/40$ and $\Delta = R_c/50$. The results for $\Delta = R_c/40$ and $\Delta = R_c/50$ were virtually indistinguishable, even for $\mathrm{De}_R > 1$ (not shown). Thus all results in this paper are based on the mesh size $\Delta = R_c/40$. It should be noted that we need to keep the CFL number lower than 0.01 in all our simulations, leading to considerable computational costs. At $\mathrm{De}_R < 1$ a larger time step can be utilized but at $\mathrm{De}_R \geq 1$, a small time step is required for smooth convergence.

Figure 4 shows viscoelastic flow streamlines through the random sphere packings at De_R=1 for solid fractions 0.3 and 0.5. The flow direction is indicated by the arrow and selected planes are colored with the normalized averaged flow velocity.

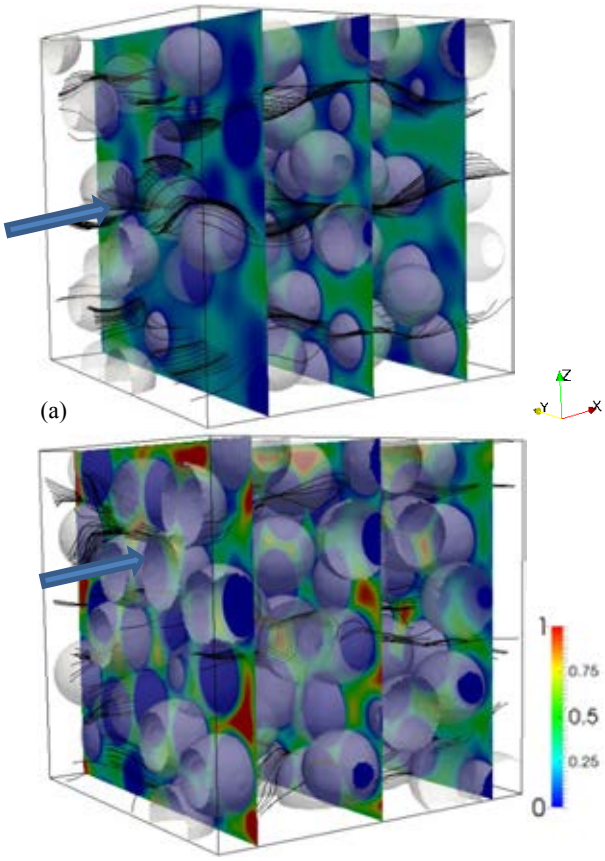

(b)

Figure 4. Viscoelastic flow streamlines through a random array of monodisperse spheres at $\mathrm{De}_R = 1.0$ for solid fractions (a) $\alpha = 0.3$ and (b) $\alpha = 0.5$. The planes are colored with normalized averaged flow velocity (arrows showing the flow direction).

These streamlines provide an idea about the complex flow heterogeneity in the porous media. For solid fraction 0.3, the flow is rather homogeneous. However for solid fraction 0.5, the pore structure triggers more tortuous flow paths and more preferential pathways.

To quantify the viscoelastic effects we use the Darcy law for flow through porous media. The volume averaged fluid velocity $\langle u \rangle$ in porous media is controlled by the pressure drop across the sample. According to Darcy's law, for a Newtonian fluid

the relation between the average pressure gradient $-\partial p / \partial x$ and the average fluid velocity across the porous medium is:

$$\left(-\frac{dp}{dx}\right) = \frac{\eta \langle u \rangle}{k} \qquad (12)$$

Here k is the permeability (units: m^2), which is related to the porosity, pore size distribution and tortuosity of the porous medium. Eq. (12) presents an operational way of measuring the permeability k by flowing a Newtonian fluid of known viscosity through the porous medium. For a viscoelastic fluid, the viscosity is not a constant but generally depends on the flow conditions. However, if we assume k is constant for a specific porous medium, we can still define an *apparent* viscosity by using Darcy's law. Dividing the apparent viscosity by its corresponding flow rate limit gives us insight in the effective flow-induced thinning or thickening of the fluid in the porous medium. In detail, the apparent relative viscosity η_{app} of a viscoelastic fluid flowing with a volumetric flow rate q and pressure drop ΔP through a porous medium is given by:

$$\eta_{app} = \frac{\left(\frac{\Delta P}{q}\right)_{VE}}{\left(\frac{\Delta P}{q}\right)_{N}} \qquad (13)$$

Figure 5 depicts how the apparent relative viscosity changes with an increase in viscoelasticity for flow through configurations with different solid fractions. With increasing De_R we initially observe a (relatively weak) flow-induced thinning. Then beyond a certain flow rate we observe a strong flow-induced thickening, which means a sharp increase in flow resistance. With increasing solid fraction (decreasing porosity), the onset of this increased flow resistance shifts to a lower De number. This shows that the increased fluid-solid interaction facilitates the onset of such a flow resistance. Experimental evidence of this increase in apparent relative viscosity was previously reported in literature [5], especially for packed bed systems.

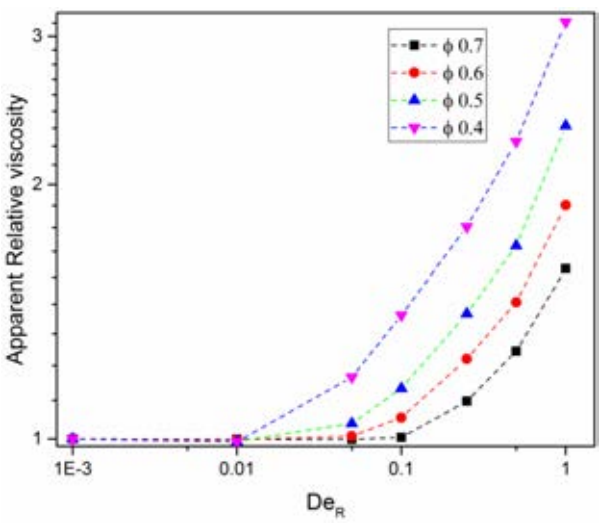

Figure 5. Apparent relative viscosity versus De_R number for different porosity ϕ. Here De_R is based on the radius R_c of the sphere.

The pore porosity and pore geometry are very important for the increase in apparent relative viscosity, but this is not reflected in the De_R number based on the radius of the spheres. Therefore, we next try to use the square root of the permeability, $\sqrt{k}$ obtained from Newtonian flow simulations, as the characteristic length scale. This altered Deborah number is defined as $De_k = \frac{\lambda U}{\sqrt{k}}$. Figure 6 shows the apparent relative viscosity versus De_k for different solid fractions. We find a collapse of all data sets of figure 4 to a single curve for the entire range of De_k numbers. This is remarkable considering the fact that, despite the different arrangement of pore structures for the different porosities, the resulting increase in flow resistance follows the same universal thickening behaviour. However, we should keep in mind that these results are strictly only valid for a FENE-P type of fluid with $L^2 = 100$ flowing through a random array of monodisperse spheres.

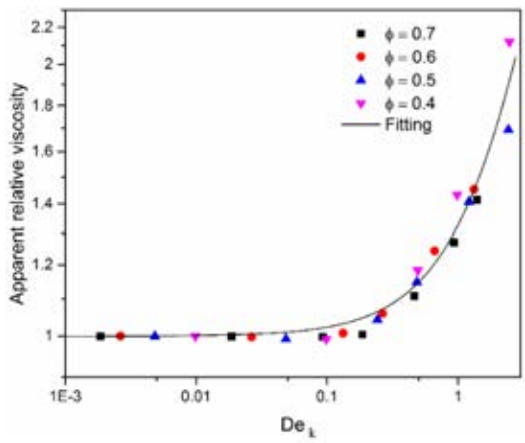

Figure 6. Apparent relative viscosity versus altered De_k, using $\sqrt{k}$ as the characteristic length scale, for different solid fractions. Neglecting the slight flow-induced thinning around $De_k = 0.1$, most data can be fitted through the correlation

$$\eta_{app} = 1 + 0.32 De_k^{1.15}.$$

CONCLUSION

We have employed a finite volume - immersed boundary methodology to study the flow of viscoelastic fluids through an array of randomly arranged equal-sized spheres representing a three dimensional disordered porous medium, for a range of solid fractions (or porosities). Irrespective of the solid fraction, we found a strong increase in flow resistance after a critical De number is reached. The increase in apparent relative viscosities measured for different solid fractions overlap with each other if the Deborah number is chosen with a length scale based on the permeability of the pore space (more precisely, $De_k = \frac{\lambda U}{\sqrt{k}}$, with k the permeability of the medium for a Newtonian fluid. The flow profile suggest that with increasing viscoelasticity the flow become more asymmetric, and increasingly preferential flow paths are found.

A more detailed study of the flow topology (not given here) shows that for the porous media investigated in our study, shear

flow becomes more important than extensional or rotational flow at higher De number. So, even though the flow is shear dominated and the shear rheology is shear thinning, the apparent viscosity from a porous medium can be flow thickening. The likely cause of this thickening is the increased heterogeneity of the flow pattern, which is related to so-called elastic turbulence, and causes more energy dissipation.

More generally, simulations such as shown here help us to understand the complex interplay between the fluid rheology and pore structure in porous media. In our future work we will study flow through three dimensional realistic porous media which have a larger distribution in pore and throat sizes.

5. Acknowledgement

This work is part of the Industrial Partnership Programme (IPP) 'Computational sciences for energy research' of the Foundation for Fundamental Research on Matter (FOM), which is part of the Netherlands Organisation for Scientific Research (NWO). This research programme is co-financed by Shell Global Solutions International B.V. This work was carried out on the Dutch national e-infrastructure with the support of SURF Cooperative.

References

1. De, S., Das, S., Kuipers, J.A.M., et al. (2016) A coupled finite volume immersed boundary method for simulating 3D viscoelastic flows in complex geometries. *J. Nonnewton. Fluid Mech.*, **232**, 67–76.
2. Dullien, F.A.L. (1979) *Porous Media-Fluid Transport and Pore Structure*, Academic, New York.
3. Lake, L.W., Johns, R.T., Rossen, W.R. and Pope, G. (1986) *Fundamentals of enhanced oil recovery.*, Society of Petroleum Engineers.
4. Soulis, J. V., Giannoglou, G.D., Chatzizisis, Y.S., et al. (2008) Non-Newtonian models for molecular viscosity and wall shear stress in a 3D reconstructed human left coronary artery. *Med. Eng. Phys.*, **30** (1), 9–19.
5. Chhabra, R.P., Comiti, J., and Macha, I. (2001) Flow of non-Newtonian fluids in fixed and fluidised beds. *Chem. Eng. Sci.*, **56** (1), 1–27.
6. Savins, J.G. (1969) Non-Newtonian Flow Through Porous Media. *Ind. Eng. Chem.*, **61** (10), 18–47.
7. Tiu, C., Zhou, J.Z.Q., Nicolae, G., et al. (1997) Flow of viscoelastic polymer solutions in mixed beds of particles. *Can. {J}. {C}hem. {E}ng.*, **75** (1 993), 843–850.
8. Zami-Pierre, F., De Loubens, R., Quintard, M., and Davit, Y. (2016) Transition in the Flow of Power-Law Fluids through Isotropic Porous Media. *Phys. Rev. Lett.*, **117** (7), 1–5.
9. Pearson, J.R. a., and Tardy, P.M.J. (2002) Models for flow of non-Newtonian and complex fluids through porous media. *J. Nonnewton. Fluid Mech.*, **102**, 447–473.
10. Sochi, T. (2007) Pore-Scale Modeling of Non-Newtonian Flow in Porous Media. *October*, **89** (October), 1–2.
11. Singh, J.P., Padhy, S., Shaqfeh, E.S.G., and Koch, D.L. (2012) Flow of power-law fluids in fixed beds of cylinders or spheres. *J. Fluid Mech.*, **i** (2012), 1–37.
12. Duda, J.L., Hong, S.A., and Klaus, E.E. (1983) Flow of polymer solutions in porous media: inadequacy of the capillary model. *Ind. Eng. Chem. Fundam.*, **22** (3), 299–305.
13. Marshall, R.J., and Metzner, a. B. (1967) Flow of Viscoelastic Fluids through Porous Media. *Ind. Eng. Chem. Fundam.*, **6** (3), 393–400.
14. Christopher, R.H., and Middleman, S. (1965) Power-law flow through a packed tube. *Ind. Eng. Chem. Fundam.*, **4**, 422–426.
15. Bruschke, M. V., and Advani, S.G. (1993) Flow of generalized Newtonian fluids across a periodic array of cylinders. *J. Rheol.*, **37** (3), 479–498.
16. Dazhi, G., and Tanner, R.I. (1985) The drag on a sphere in a power-law fluid. *J. Nonnewton. Fluid Mech.*, **17** (1), 1–12.
17. Shahsavari, S., and McKinley, G.H. (2015) Mobility of power-law and Carreau fluids through fibrous media. *Phys. Rev. E - Stat. Nonlinear, Soft Matter Phys.*, **92** (6), 1–27.
18. Morais, A.F., Seybold, H., Herrmann, H.J., and Andrade, J.S. (2009) Non-Newtonian Fluid Flow through Three-Dimensional Disordered Porous Media. *Phys. Rev. Lett.*, **103** (19), 1–5.
19. Liu, H.L., Moon, J.S., and Hwang, W.R. (2012) Numerical simulation of a shear-thinning fluid through packed spheres. *Korea Aust. Rheol. J.*, **24** (4), 297–306.
20. Sullivan, S.P., Gladden, L.F., and Johns, M.L. (2006) Simulation of power-law fluid flow through porous media using lattice Boltzmann techniques. *J. Nonnewton. Fluid Mech.*, **133** (2–3), 91–98.
21. Liu, A.W., Bornside, D.E., Armstrong, R.C., and Brown, R.A. (1998) Viscoelastic flow of polymer solutions aroud a periodic, linear array of cylinders: comparisons of predictions for microstruture and flow fields. *J. Nonnewton. Fluid Mech.*, **77**, 153–190.
22. Richter, D., Iaccarino, G., and Shaqfeh, E.S.G. (2010) Simulations of three-dimensional viscoelastic flows past a circular cylinder at moderate Reynolds numbers. *J. Fluid Mech.*, **651**, 415–442.
23. Talwar, K.K. (1992) Application of higher order finite element methods to viscoelastic flow in porous media. *J. Rheol. (N. Y. N. Y).*, **36** (7), 1377.
24. Alcocer, F.J., and Singh, P. (2002) Permeability of periodic arrays of cylinders for viscoelastic flows. *Phys. Fluids*, **14** (7), 2578–2581.
25. Souvaliotis, A., and Beris, A.N. (1996) Spectral collocation/domain decomposition method for viscoelastic flow simulations in model porous geometries. *Comput. Methods Appl. Mech. Eng.*, **129** (1–2), 9–28.
26. Galindo-Rosales, F.J., Campo-Deao, L., Pinho, F.T., et al. (2012) Microfluidic systems for the analysis of viscoelastic fluid flow phenomena in porous media. *Microfluid. Nanofluidics*, **12** (1–4), 485–498.
27. Chmielewski, C., and Jayaraman, K. (1993) Elastic instability in crossflow of polymer solutions through periodic arrays of cylinders. *J. Nonnewton. Fluid Mech.*, **48** (3), 285–301.
28. Gupta, R.K., and Sridhar, T. (1985) Viscoelastic effects in non-Newtonian flows through porous media. *Rheol. Acta*, **24** (2), 148–151.
29. R. B. Bird, R. C. Armstrong, O.H. (1987) *Dynamics of Polymeric Liquids*.
30. Guénette, R., and Fortin, M. (1995) A new mixed finite element method for computing viscoelastic flows. *J. Nonnewton. Fluid Mech.*, **60** (1), 27–52.
31. Daan Frenkel and Berend Smit (2001) *Understanding Molecular Simulation From Algorithms to Applications*.
32. Noya, E.G., Vega, C., and De Miguel, E. (2008) Determination of the melting point of hard spheres from direct coexistence simulation methods. *J. Chem. Phys.*, **128** (15), 1–7.
33. N. Kumar, O. I. Imole, V. Magnanimo, S. Luding

(2012) Deformation Modes for Assemblies of Frictionless Polydisperse Spheres. *Adv. Mater. Res.*, **508**, 160–165.

34. Tang, Y., Kriebitzsch, S.H.L., Peters, E.A.J.F., et al. (2014) A methodology for highly accurate results of direct numerical simulations: Drag force in dense gas-solid flows at intermediate Reynolds number. *Int. J. Multiph. Flow*, **62**, 73–86.